Advanced Optical Materials / Volume 11, Issue 16 / 2300180

Research Article | Full Access

Tailoring the Phonon Polaritons in α-MoO_3 via Proton Irradiation

Ya-Nan Zhang, Yuanjun Tang, Liujian Qi, Yanze Feng, Mengda Li, Junru An, Lei Wang, Huiping Zhu, Bo Li, Dabing Li, Shaojuan Li

First published: 17 May 2023
https://doi-org.fgul.idm.oclc.org/10.1002/adom.202300180

Abstract

Phonon polaritons (PhPs) provide new prospects for the development of next generation nanophotonic devices due to the high optical confinement, low optical losses, and long lifetime. It is crucial to modulate the PhPs in already discovered materials in order to utilize PhPs efficiently and increase the device operability. In this work, oriented particle trace structures in α-MoO_3 are generated where the dielectric functions are broken by proton irradiation. Those particle trace structures act as in-plane boundaries, launching and reflecting PhPs. In-plane needle-like PhPs in the intermediate state are obtained and finally the switching-off of PhPs via increasing the irradiation fluences is achieved. Furthermore, the switching-off PhPs are partly restored to original state by annealing. The method provides an opportunity to manipulate light at the nanoscale and construct in-plane PhPs reflectors with the potential to be used for polaritonic devices and circuits.

1 Introduction

Phonon polaritons (PhPs) are half-light, half-matter quasiparticles that originate from strong coupling between light and phonons, featuring with low optical losses, strong light confinement, long lifetime, and high-quality factors.[1-4] These merits endow it great potential in a variety of polaritonic applications, such as imaging,[5] molecular detection,[6, 7] hyperlensing,[5, 8, 9] sensing[10, 11] and waveguiding.[12, 13] Up to now, a lot of research about PhPs has been conducted on the bulk polar dielectric crystals, such as SiC,[14, 15] SiO_2,[16, 17] $CdWO_4$,[18] and Ga_2O_3.[19] Recently, two-dimensional (2D) van der Waals (vdWs) crystals as naturally anisotropic materials have provided an excellent new material platform for PhPs research.[13, 20-23] Their naturally anisotropic characteristics origin from highly oriented lattice vibrations in the in-plane and out-of-plane directions with strong covalent bonds and weak interlayer vdWs forces, respectively, which imply different optical properties along these two directions. In principle, PhPs are sustained at the specific frequencies that

normally occur between the transverse optical (TO) and longitudinal optical (LO) frequencies of polar crystals, termed as reststrahlen bands (RBs). The RBs of a material are specific, which means that PhPs can only be launched within the fixed wavebands with specific propagation mode, drastically limiting the flexibility and applicability of PhPs. In order to utilize PhPs efficiently and increase the operability and possibilities, it is not only necessary to find and synthesize new PhPs materials, but also crucial to modulate the PhPs in already discovered materials.

Among the large family of vdWs materials, α-MoO_3 is a typical biaxial semiconductor that has aroused widespread interests in photonics.[24-26] Previous studies have shown that α-MoO_3 crystal exhibits two infrared RBs between 820 and 1010 cm^{-1}.[27,,28] Incident light with frequency within the RBs can excite anisotropic PhPs of α-MoO_3 with the assistance of antennas.[29] Thereby, α-MoO_3 has emerged as an ideal platform for studying and modulating PhPs. So far, a serious of researches related to the manipulation of PhPs have been reported. One conventional method is to change the dielectric environment by building vertical heterogeneous structures. For example, Zhang et al. constructed heterogeneous interfaces between the vdWs material and bulk polar dielectric, realizing larger confinement, steerable and unidirectional polariton excitation of PhPs.[25] Another representative method is to construct moiré superlattice by customized interlayer coupling. There are several studies showing that precise control of the dispersion of PhPs via controlling the twist angle between two stacked vdWs crystals.[30-33] Also, the PhPs can be tuned by edge engineering, that is, artificially created reflective edges with different angles to the crystal direction tailors the polaritonic patterns.[34, 35] Furthermore, an alternative approach to tune the polariton properties in 2D materials is by gate modulation, which has been widely utilized to modulate graphene plasmonics.[36-39] However, due to the wide band gap (≈3 eV) and poor electrical conductivity of α-MoO_3, the direct electric gating of α-MoO_3 is very difficult.[40] Although there are some studies using gate voltage to control the hybrid polaritons in graphene/α-MoO_3 heterojunction,[26, 41, 42] the tunability is essentially based on modulation of graphene plasmonics. In addition, the wavelengths and intensity of the PhPs can be further modulated by chemical means, including but not limited to ion intercalation.[43] Notably, in a CMOS-compatible Ge-SiC polaritonic nano-resonator, the PhP modes in the resonator can be adjusted not only by the size of the resonator, but also by chemical means (oxidizing the Ge layer and controlling the thickness of the oxide layer).[44]

Here, we propose another approach to tailor polaritons in 2D materials, that is, ion irradiation. As a kind of ion irradiation, proton irradiation produces crystal defects such as vacancies and interstitial atoms through displacement damage (knocking atoms out of their initial position), and then affecting the optical properties of materials. Highly focused proton beam has been utilized as a direct-write lithography technique to change the refractive index of the irradiated region, which can be used to fabricate micro-optical components, such as waveguides,[45-47] gratings,[48] and micro-lens arrays.[49, 50] In polaritonics, it can be used to regulate the energy distribution of the exciton polaritons in GaAs microcavity.[51]

However, the effect of proton irradiation on PhPs remain elusive so far. In our experiments, we demonstrate that proton irradiation efficiently modulates the PhPs of α-MoO_3 by generating oriented particle trace structures in the material. We obtain intermediate states with in-plane nanostructures acting as the boundaries that launch and reflect PhPs at lower proton irradiation fluences, and the intrinsic PhPs of α-MoO_3 will be turned off at higher irradiation fluences. In addition, the disappeared PhPs can be partly restored to original state via annealing. Our results provide a potential strategy to directly manipulate the lattice defects of materials for possibly tailoring properties of polaritonic devices based on PhPs.

2 Results and Discussion

In this work, all α-MoO_3 flakes were prepared by mechanical exfoliation and the bulk crystals were synthesized using chemical vapor deposition (CVD) method (see Experimental Section and Figure S1). **Figure 1a** shows the orthorhombic structure and lattice constants of α-MoO_3, in which the six nearest oxygen atoms of the molybdenum atom are not equivalence, each of the three axial lattice constant (a, b, and c) is different and the layers are bounded by vdWs forces.[52] Such a complex structure allows for the existence of multiple phonon modes which correspond to multiple obvious characteristic peaks in the Raman spectrum shown in Figure 1b, and these complex phonon modes result in multiple RBs.[12, 27] To explore the polaritonic response of α-MoO_3 flakes, we measured near-field imaging of PhPs in our samples using a scattering-type near-field optical microscope (s-SNOM). The schematic diagram of the experiment is shown in Figure 1c. The mid-infrared excitation light illuminates the vertically oscillating atomic force microscopy (AFM) tip, which acts as a nanoantenna to excite the PhPs and scatter the near field signal of α-MoO_3.[4, 36, 39] The tip-launched PhPs propagate away and then reflect back at the sample edge, interfering with the PhPs continuously launched by the tip. We imaged the PhPs of α-MoO_3 at 900 and 990 cm^{-1}, as shown in Figure 1d,e. It should be noted that the two frequencies of excitation light are in different RBs (upper RB, 962–1010 cm^{-1} and lower RB, 818–974 cm^{-1}).[43] The PhPs of α-MoO_3 only propagate along the [100] crystal direction with hyperbolic dispersion at ω = 900 cm^{-1}, and along both [100] and [001] crystal direction with elliptic dispersion at ω = 990 cm^{-1}, consistent with the previous research.[1]

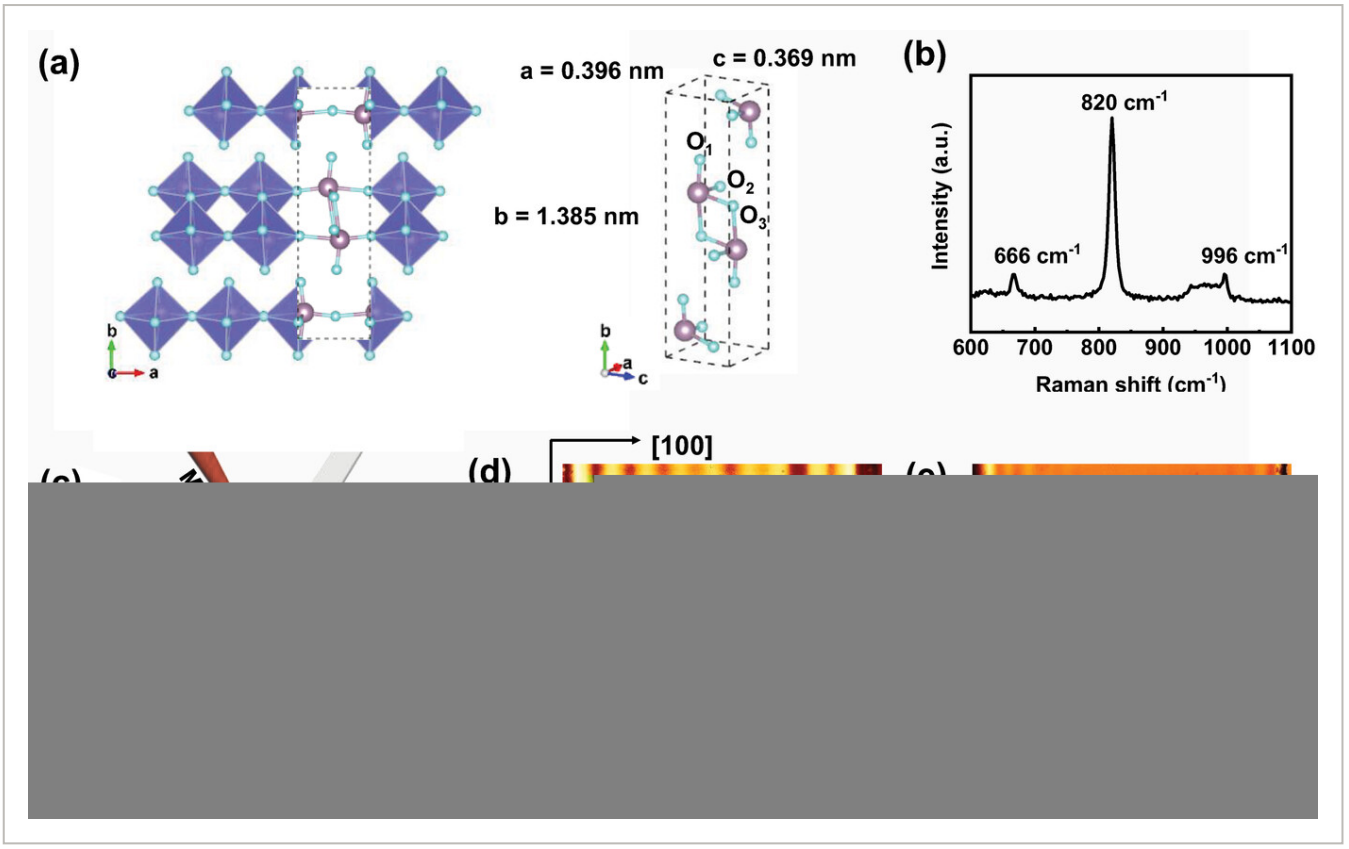

Figure 1

Open in figure viewer | PowerPoint

Structural characterizations and near-field images of α-MoO_3. a) Illustration of the orthorhombic lattice structure and the unit cell of layered α-MoO_3 (blue spheres: oxygen atoms, purple spheres: molybdenum atoms). b) Raman spectrum of α-MoO_3 flake on SiO_2/Si substrate. c) Schematic of the s-SNOM imaging configuration. d) PhPs image of α-MoO_3 flake at illuminating frequencies ω = 900 cm^{-1}. e) PhPs image of α-MoO_3 flake at illuminating frequencies ω = 990 cm^{-1}. The near-field images were obtained at the 4th harmonics oscillation frequency. Scale bar = 2 μm.

We investigated the PhPs of α-MoO_3 flakes with similar thicknesses before and after exposing to 150 keV proton irradiation with different fluences. All α-MoO_3 flakes in this study are about 130 nm in thickness (AFM images are shown in Figure S2, Supporting Information). **Figure** 2a–e shows the near-field amplitude images of α-MoO_3 flakes at 990 cm^{-1} before and after proton irradiation with fluences of 5×10^{12}, 5×10^{13}, 5×10^{14}, 1×10^{15}, and 1×10^{16} particles cm^{-2} (p cm^{-2}) (the corresponding near-field images before and after irradiation at 900 cm^{-1} are shown in Figure S3, Supporting Information, and the near-field images of more samples are shown in Figure S4, Supporting Information). The PhPs changed regularly with the increase of proton fluences. As described previously, for α-MoO_3 without irradiation, we observed the interference fringes of PhPs propagating parallel to the [001] and [100] directions at 990 cm^{-1}. As the irradiation fluence increases, highly oriented oblique crossed PhPs are obtained in the intermediate state, and finally the PhPs are turned off (Figure 2). The intrinsic PhPs interference fringes of α-MoO_3 irradiated with

proton fluences of 5×10^{12} p cm^{-2} are unchanged and consistent with the original state (Figure 2a and Figure S3a, Supporting Information). For the sample irradiated with proton fluences of 5×10^{13} p cm^{-2}, some slight dotted PhPs appeared in the near-field amplitude image at 990 cm^{-1} (Figure 2b and Figure S4a, lower panel, Supporting Information) but were not observed at 900 cm^{-1} (Figures S3b and S4a, upper panel, Supporting Information). Obviously, the PhPs of α-MoO_3 at 990 cm^{-1} are more sensitive to defects than those at 900 cm^{-1}. And for the sample irradiated with proton fluences of 5×10^{14} and 1×10^{15} p cm^{-2}, we can clearly observe the needle-like polaritons at both 900 and 990 cm^{-1} (Figure 2c,d, Figure S3c,d, Supporting Information). Notably, the needle-like polaritons are at a fixed angle to the [001] direction appear on the whole flake, and the intrinsic PhPs exist across the sample simultaneously. The similarity of the PhPs at these two irradiation fluences suggests that the conditions for producing such PhPs are not harsh. However, for the sample irradiated with a higher proton fluences of 1×10^{16} p cm^{-2}, PhPs were switched off in the near-field image as seen in Figure 2e, in which neither needle-like polaritons nor intrinsic PhPs can be observed. Similar phenomena have been reported for the construction of oriented in-plane boundaries through the hydrogenation of α-MoO_3 to further modulate PhPs.[40, 53] According to previous report, short hydrogenation time produced needle-like PhPs, and long hydrogenation time turned off intrinsic PhPs. The oriented hydrogenation behavior of α-MoO_3 has also been reported in another literature.[54]

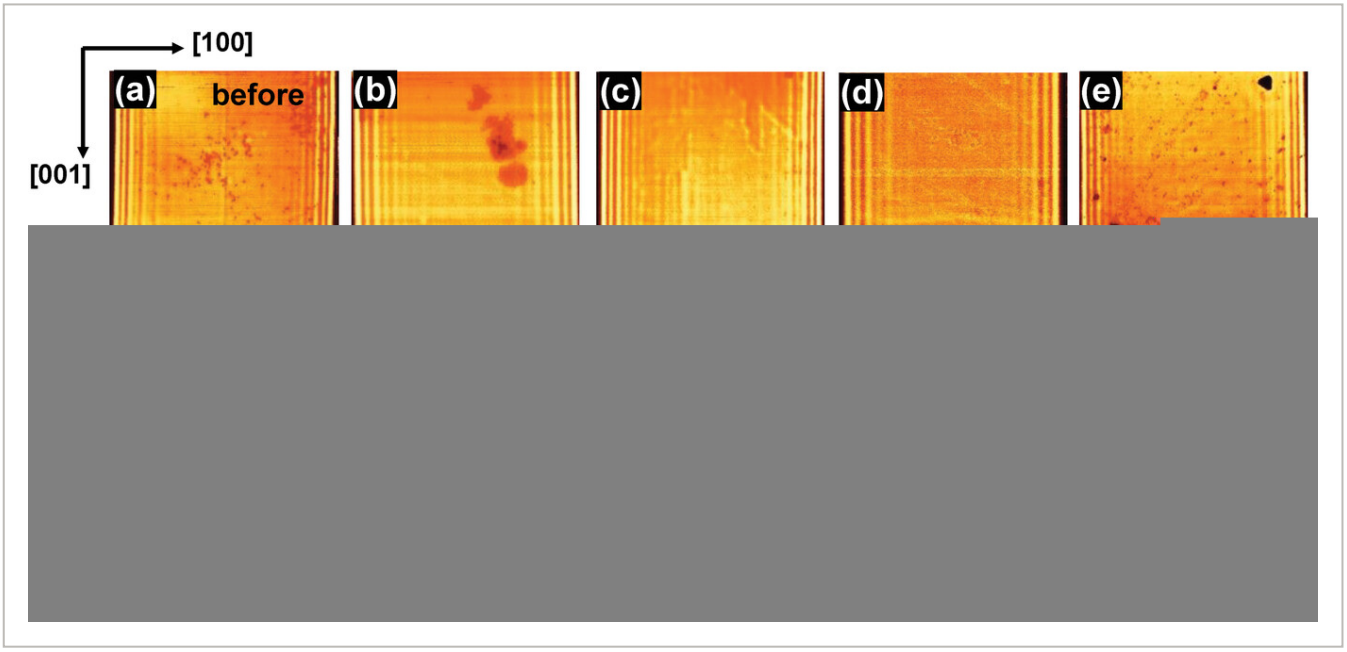

Figure 2

Open in figure viewer | PowerPoint

Gradient evolution of PhPs with increasing fluences of proton irradiation at 990 cm^{-1}. Near-field images of α-MoO_3 flakes taken at 990 cm^{-1} before (top) and after (bottom) irradiation with different irradiation fluences of a) 5×10^{12}, b) 5×10^{13}, c) 5×10^{14}, d) 1×10^{15}, and e) 1×10^{16} p cm^{-2}, respectively. The near-field images were obtained at the 4th harmonics oscillation frequency. Scale bar = 2 μm.

To explore the physical origin of the needle-like polaritons in our experiments, we further investigated the distribution of these patterns in our samples. **Figure** 3a shows s-SNOM near-field amplitude images of the α-MoO_3 flake with proton fluences of 5×10^{14} p cm^{-2} at ω = 900 and 990 cm^{-1}. We extracted the amplitude profiles along the dashed lines indicated in Figure 3a which are parallel to the direction of needle-like PhPs propagation (Figure 3b). These dashed lines are selected from the middle area of the image, away from the edges, to avoid the influence of intrinsic PhPs on the traces of the needle-like PhPs. We found that the extracted amplitude profiles did not exhibit a constant period (more amplitude profiles are shown in Figure S5, Supporting Information). The corresponding topography images of this flake before and after irradiation are shown in Figure 3c. The root mean square (RMS) roughness extracted from the red rectangular area are 0.67 (left) and 0.63 nm (right) before and after irradiation, indicating that the irradiation did not result in evident topography damage. The slight difference may be caused by the AFM images measurement process. We further extracted height profiles of the irradiated flake from Figure 3c along the black dashed lines which are also parallel to the propagation direction of needle-like PhPs. The height profiles were extracted from six different dash lines at different regions to ensure the reliability. All height variations of AFM profiles are less than 1 nm (more height variations profiles are shown in Figure S6, Supporting Information). In fact, such small height variations hardly launch and reflect PhPs, and cannot contribute to near-field signal.[53] Therefore, we can conclude that the sharp needle-like fringes are most possibly derived from the PhPs reflected at the in-plane boundaries where the dielectric function changes, rather than the topographic changes of α-MoO_3 flake. We give the following explanation for above phenomenon: proton irradiation generated directed oxygen dislocation, which causes the directed changes of local dielectric function and forms in-plane boundaries to launch and reflect PhPs. When the irradiation fluence is large enough, the boundaries generated by the irradiation become denser, causing irregular scattering of PhPs, which leads to unobservable reflection, as previously demonstrated in Figure 2. The above process will be further elucidated in the following part.

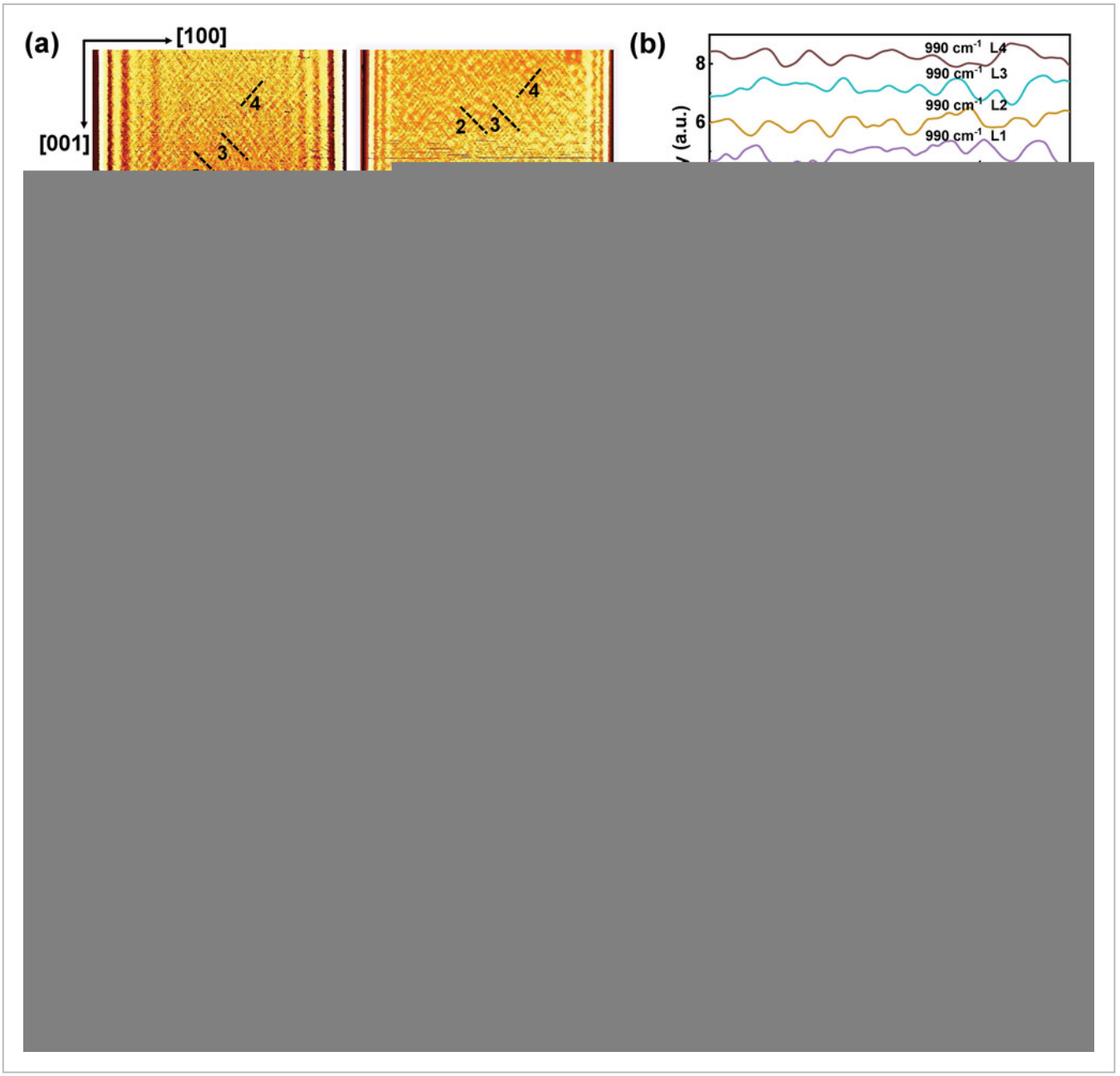

Figure 3

Open in figure viewer | PowerPoint

Needle-like PhPs in two RBs. a) PhPs irradiated with proton fluences of 5×10^{14} p cm^{-2} at 900 cm^{-1} (left) and 990 cm^{-1} (right). Scale bar = 2 μm. b) Line profiles extracted from the near-field amplitude images along the dashed lines L1, L2, L3, and L4 indicated in (a). The amplitude profiles in (b) were normalized. c) AFM images before (left) and after (right) irradiation. Scale bar = 2 μm. d) Height profiles extracted from the AFM images along the dashed lines L1, L2, L3, L4, L5, and L6 indicated in (c). e) 2D Fourier analysis of (a). The white circule indicates the results of pristine MoO_3 before irradiation. f) Fourier analysis of (b). The near-field images were obtained at the 4th harmonics oscillation frequency.

It is worth pointing out that the difference between the near-field images at 900 and 990 cm^{-1} also prove that the near-field needle-like structures are not simply the fingerprints

of the boundaries produced by proton irradiation (Figure 3a and Figure S5, Supporting Information). After irradiation, two adjacent opposite boundaries can form a microcavity in which the PhPs standing waves were constrained. The size of the microcavity determines the PhPs patterns.[34, 44, 55] To prove this, we performed Fourier transform of the near-field images. The Fourier transform of the left and right parts in Figure 3a showed in two different distributions in *k*-space (Figure 3e). The energy distribution within the white ellipse correspond to the intrinsic PhPs of α-MoO_3 before irradiation, while the high-frequency component outside the ellipse came from the contribution of the needle-like PhPs. The energy of these high-frequency components is not scattered but symmetrically distributed in the four quadrants of *k*-space, showing certain directionality and reflecting the regular orientation of real space needle-like PhPs. Due to the very short and densely distributed needle-like PhPs just after irradiation over the entire sample, there is a slight dispersion of high-frequency components in 2D Fourier analysis. As time goes on, the distribution of the high frequency component in Fourier space becomes more concentrated (Figure S7, Supporting Information). Figure 3f shows the Fourier transform analysis of the line profiles in Figure 3b, which contained several peaks, indicating that the period is complex. The peak positions in each curve were different, because the dotted lines indicated in Figure 3a span several microcavities with different lengths caused by the different boundary distributions, and the PhPs modes constrained in each microcavity may be different.

The proton irradiation method directly manipulated the lattice defects of α-MoO_3 to modify PhPs, and obtained non-volatile results at room temperature. However, the defects generated by irradiation will continue to migration over a period of time,[56] resulting in continuous changes in the size and location of the in-plane microcavity, as well as the distribution of needle-like PhPs. As observed, the spatial density of needle-like PhPs becomes smaller and the length and width become larger over time after being placed in nitrogen atmosphere for a period of time (Figure S7, Supporting Information), corresponding to the defect migration stage. In Figure S7d (Supporting Information), we found fringes with similar distribution in the same region of the sample at 900 and 990 cm^{-1} (within the blue dotted line), possibly containing the boundaries produced by proton irradiation. A zoomed view of the area within the blue dashed line of the top image in Figure S7d (Supporting Information) is shown in Figure S8 (Supporting Information). The needle-like structure within the black dashed line in Figure S8c (Supporting Information) possibly contains in-plane boundary and the width is less than 200 nm. Notably, the physical size of this fringe cannot be equated with the size of the proton-written domains, because near-field information is formed by PhPs reflecting at adjacent opposite boundaries.

Notably, for the samples treated with irradiation fluences of 1×10^{16} p cm^{-2}, the large irradiation fluence leads to large lattice defects restraining the intrinsic PhPs of α-MoO_3 (**Figure** 4a,b). In that case, repairing the lattice defects should restore the intrinsic PhPs. Thus, we conducted annealing experiments on the irradiated samples at 350 °C. During annealing, nitrogen was used as the protective gas, and an appropriate amount of oxygen

was introduced to repair the oxygen vacancies possibly generated during the irradiation. The crystal structures of the irradiated α-MoO_3 relaxed via annealing and the intrinsic PhPs were partly restored in both RBs, as shown in Figure 4c. Thus, we achieved the switch of PhPs by manipulating the lattice of α-MoO_3. Furthermore, the near-field amplitude line profiles along the dash line marked in Figure 4a–c are extracted, as displayed in Figure 4d,e. It should be noted that the wavelength of PhPs at 900 cm^{-1} became shorter after switching off and switching on, while the wavelength of PhPs at 990 cm^{-1} became longer. The interference fringes periods are 569 and 520 nm at 900 cm^{-1} before irradiation and after annealing, respectively. And at 990 cm^{-1}, the corresponding values are 280 and 330 nm, respectively. The momenta changes observed before and after annealing in our experiments may be due to that the defects in the α-MoO_3 crystal are not completely repaired during the annealing process. The main parameters that affect the annealing quality include atmosphere environment, heating rate, annealing temperature, holding time and cooling rate, etc. Therefore, finding the perfect annealing parameters in the experiment worths further investigation in the future.

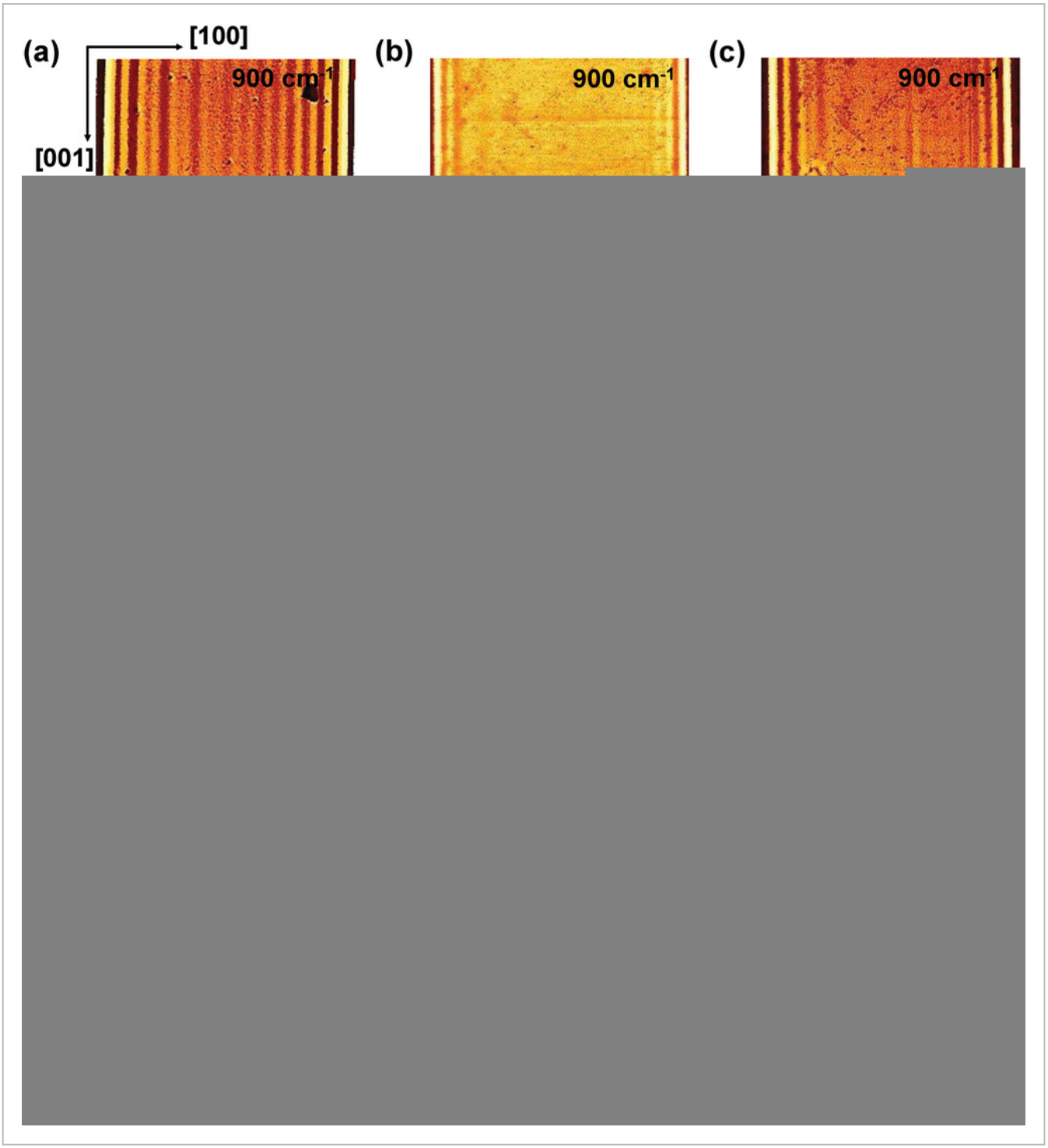

Figure 4

Open in figure viewer | PowerPoint

Non-volatile modulation and reversible switching of PhPs in two RBs of α-MoO_3. a–c) Near-field images of the switching process at 900 cm^{-1} (top) and 990 cm^{-1} (bottom), origin (a), switch off (b), switch on (c). Scale bar = 2 μm. d,e) Near-field amplitude profiles extracted from the dash lines indicated in (a–c). The amplitude profiles in (d,e) were normalized.

To understand the generation mechanism of the needle-like PhPs in the post-irradiated α-MoO_3, it is important to have a deep insight into the interaction process between protons

and lattice atoms in α-MoO_3. The SRIM simulator is a kind of software that can simulate the interaction process and give the damage situation in α-MoO_3.[57] Energetic ions collide with lattice atoms, then cause these atoms to leave the lattice positions and create vacancies. These vacancies are the tracks left by the ions as they pass through the materials. The atom that leaves its lattice position and forms a vacancy is called recoil atom. Usually, the recoil atom has high energy, and can collide with the atoms around it to create vacancies. These vacancies reflect the track of the recoil atom. **Figure 5b** shows the particle tracks generated by incidence of protons into the stacked material of α-MoO_3/SiO_2/Si simulated using SRIM, with the schematic diagram of the proton irradiation experiment shown in Figure 5a. In Figure 5b, the white dots represent the tracks of the protons, and the colored dots represent the tracks of the recoil atoms in each material layer. From the simulation result, we know that the particle tracks form a distribution with a certain width around the direction of high-energy proton incidence, suggesting that vacancies generated by collisions are distributed within a certain width.

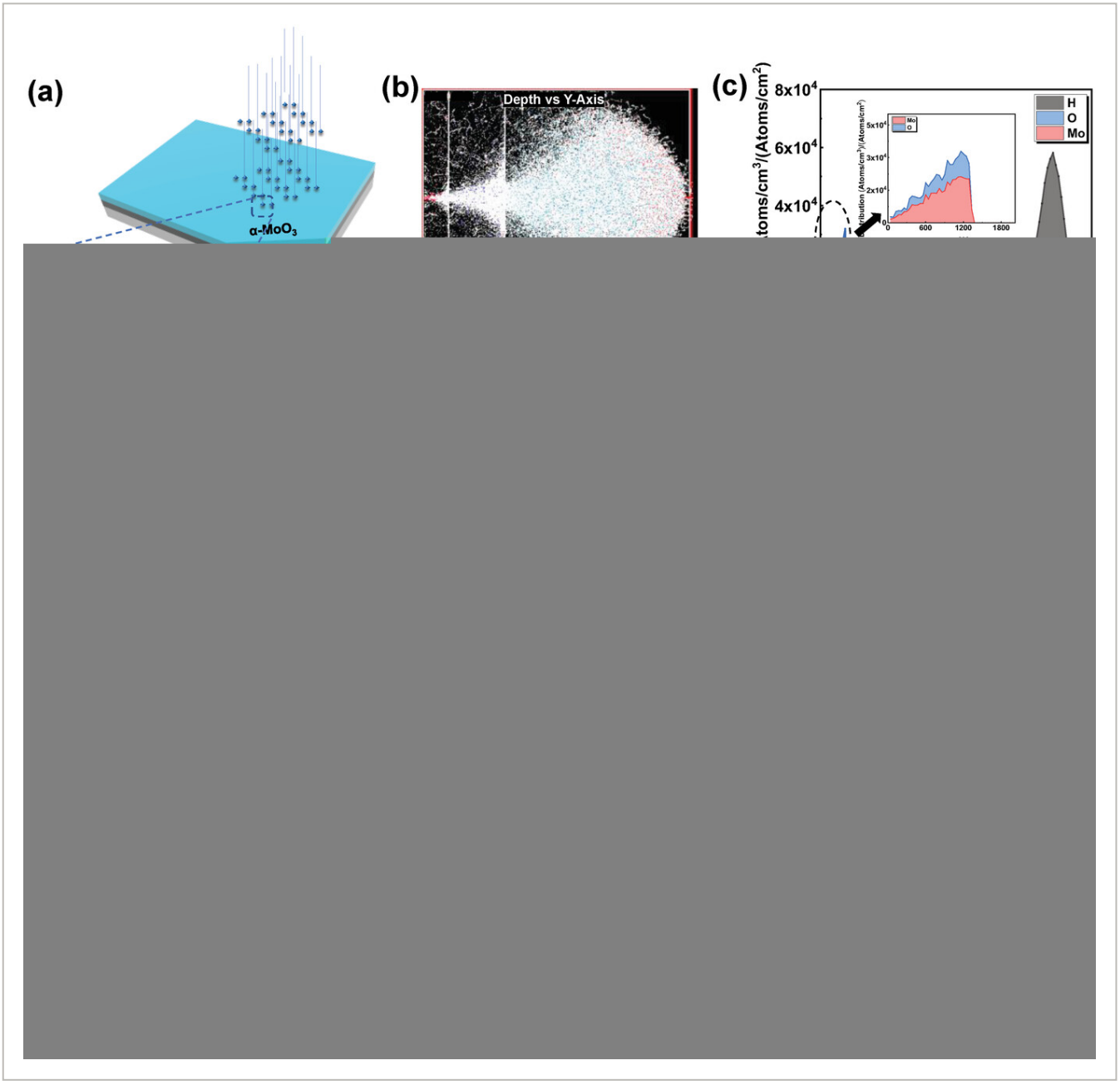

Figure 5

Calculation and mechanism explanation of irradiation process of α-MoO_3. a) Schematic illustrations of the proton irradiation. b) Particle ranges image obtained from SRIM calculation (from left to right are 130 nm MoO_3, 300 nm SiO_2, and 1000 nm Si. The red dots, dark blue dots, light blue dots, and orange dots represent the distribution of Mo atoms, Si atoms in SiO_2 layer, Si atoms in Si layer, and H atoms respectively). c) Distribution of defects with depth. d) Raman spectra before and after irradiation. e) XRD spectra before and after irradiation. f) Relative formation energy of oxygen vacancies (Vo). g) Relative formation energy of dioxygen vacancy system. h) Schematic illustrations of possible tracks of protons. i) Schematic diagram of possible cascade collisions in the first quadrant of the Cartesian coordinate system.

Figure 5c shows the distribution of the protons and the recoil atoms of O and Mo with the sample depth. It can be seen that the protons with energy of 150 keV penetrate the α-MoO_3 and SiO_2 layers and deposit in the Si substrate layer. This result indicates that it is impossible for protons to become intercalation atoms within α-MoO_3 interlayer, and introduce needle-like PhPs as the case in hydrogenation of α-MoO_3.[40, 53] At the same time, by characterizing the Raman and X-ray diffraction (XRD) spectrum of α-MoO_3 before and after irradiation, as shown in Figure 5d,e, it is also found that the characteristic peaks of α-MoO_3 are almost unchanged after irradiation, implying that the damage in α-MoO_3 crystallinity is not serious. This phenomenon also indirectly confirms that protons cannot exist in large quantities within α-MoO_3 interlayer, becoming intercalation atoms and thereby regulating the PhPs in α-MoO_3. Then, the occurrence of the needle-like PhPs in the post-irradiated α-MoO_3 is most possibly caused by the defective structure induced by proton irradiation. Figure 5c shows that during the irradiation process, the number of O recoil atoms is significantly greater than that of Mo recoil atoms, especially in the region where protons and lattice atoms collide most seriously. In this region, the number of O recoil atoms is about 1.5 times that of the Mo recoil atoms. And generally, atoms with larger masses have higher displacement threshold energy.[58] Generating a displced Mo atom requires overcoming a large displacement threshold energy. The displacement of Mo atoms generated in the subsequent cascade collision process is relatively small. Therefore, the displaced O atoms have a greater impact on the dielectric function.

In order to further specify the microscopic process of interaction between protons and O atoms in MoO_3, first-principles calculations were carried out. The inset in Figure 5f shows the primitive structure of the α-MoO_3, and three different types of O atoms, labeled O_1, O_2, $O_{2'}$, O_3 and $O_{3'}$, in the primitive structure. The formation energy of the oxygen vacancies formed by these three types of O atoms was calculated, as shown in Figure 5f. The formation energy of Vo at the position of O_1 is significantly smaller than those of Vo at the other positions, indicating that O atoms located at the interlayer position are more likely to be knocked out to form recoil atoms under the collision of protons. Due to its high energy, the recoiled O atom can still collide with other interlayer O atoms around it and produce more Vo. We

calculated the defect formation energy of two V_O produced by the collision of the O recoil atom and its nearby O atoms. Figure 5g shows a diagram of how this formation energy vary with the distance between the two V_O. It clearly suggests that the formation energy of the two V_O with the smallest distance, that is, the closest neighbors, is significantly greater than those of the two V_O with larger distance. Additionally, the formation energy difference between the other two V_O is not much. We can infer that the O atoms with a certain distance from the O recoil atoms are prone to form vacancies if they are collided with the O recoil atoms. Thus, it can be deduced that collisions are not carried out in a specific direction, but within a certain width. This is similar to the incident of protons into the material to form a track within a certain width, as displayed in Figure 5b. Along the direction of the O recoil incident path, the crystal structure of the O atoms located in the interlayer changes significantly, eventually resulting in the generation of the needle-like PhPs in α-MoO_3 in the near-field images.

Figure S9 (Supporting Information) is a characterization of the needle-like PhPs in α-MoO_3 in a smaller scale. It clearly shows that the adjacent needle-like PhPs cross at a certain angle (80 ± 2°). This implies when the O recoil atoms collide with other interlayer O atoms, although the tracks are within a width, but also in a certain direction. In the primitive cell, there are four kinds of interlayer O atoms with their chemical bonds in the four quadrants of the Cartesian coordinate system, as shown in Figure 5h. Here, we assign these O atoms as O^1_{inter}, O^2_{inter}, O^3_{inter}, and O^4_{inter}, respectively. Figure 5h also represents two possible tracks of protons. We can see that when the protons are incident into α-MoO_3, they may collide with O^1_{inter}, O^2_{inter}, O^3_{inter}, and O^4_{inter} in their path. Since the chemical bonds related with the four O atoms point to the four quadrants and are axisymmetrically distributed, after the protons collide with them, these four types of O recoil atoms will move toward to four quadrants in plane, and form tracks distributed axisymmetrically in plane, as shown in Figure 5i. As a result, a large number of needle-like PhPs intersected at the angle of 80 ± 2° in the near-field images are observed in Figure S9 (Supporting Information). This phenomenon further verifies the proposed interpretation of the microscopic behavior of protons colliding with O atoms in α-MoO_3, which leads to the cascade collisions within a certain width, and thereby induces the appearance of the needle-like PhPs in α-MoO_3.

3 Conclusion

In this work, we demonstrated a potential strategy for the manipulation of the PhPs of α-MoO_3 by proton irradiation-induced oriented lattice defects. The proton irradiation method can establish regular and highly oriented in-plane heterostructures which launch and reflect PhPs. Furthermore, reversible switching of PhPs is achieved via annealing. The process of proton irradiation on α-MoO_3 was revealed by SRIM and first-principles calculations: proton irradiation tends to break the bonds between Mo and interlayer O atoms (Mo-O_1). Protons more likely knock the O atoms located at the interlayer position away from the initial positions, and the recoiled O atom will collide with other interlayer O atoms around it and

produce more Vo, which in turn produce oriented boundaries where the dielectric functions change to reflect and launch PhPs. Our strategy provides a new platform to tailor the PhPs of vdWs materials for possible application of polaritonic devices.

4 Experimental Section

Preparation of α-MoO_3 Flakes

CVD method was applied to synthesize high-quality α-MoO_3. Firstly, SiO_2/Si substrates were ultrasonically cleaned by using deionized water (for 10 min), acetone (for 10 min), and ethanol (for 10 min) separately. As shown in Figure S1a (Supporting Information), 0.3 g MoO_3 powder was placed in the heating zone of the quartz tube, and six pieces of SiO_2/Si substrates were placed downstream of the MoO_3 powder with different distances. Before heating, the quartz tube was cleaned by high-purity Ar for 10 min. Then the quartz tube was heated to 785 °C in 60 min and was maintained at 785 °C for 60 min for the growth of high-quality α-MoO_3 with Ar (50 sccm) as the carrier gas, after which, the tubular furnace system was cooled down naturally to room temperature.

Proton Irradiation

The proton irradiation experiments were completed using space integrated irradiation equipment at the Laboratory of Materials Behavior and Evaluation Technology in Space Environment of Harbin Institute of Technology. The proton energy was 150 keV and the proton irradiation fluences were 5×10^{12}, 5×10^{13}, 5×10^{14}, 1×10^{15}, and 1×10^{16} p cm^{-2}, respectively.

Characterization

Raman spectra were collected with a commercial confocal microscope system (WITec, alpha 300r). The excitation light wavelength was 532 nm during measurements. The surface topography and near-field amplitude images were measured using a commercial s-SNOM (neaSNOM). The AFM tip (NanoWorld, Arrow-NCPt) was tapped at an amplitude of 80 nm and a frequency of 270 kHz. XRD spectra were tested using Powder X-Ray Diffractometer (BRUKER, D8 Focus).

Sample Annealing

The annealing temperature was set as 350 °C at a rising rate of 1 °C s^{-1}. The nitrogen and oxygen fluxes were 200and 50 sccm, respectively. The oxygen was turned off at the end of annealing and the nitrogen was continuously introduced at a flux of 200 sccm until it cooled naturally to room temperature.

Simulation and Calculation

Particle ranges and defect distribution were obtained from Stopping and Range of Ions in Matter (SRIM) calculation.[57] Defective system energy was obtained by density functional theory (DFT) as implemented in Vienna ab initio simulation package (VASP).[59] Generalized gradient approximation was employed as the exchange-correlation potential with the Perdew–Burke–Ernzerhof parameterization method.[60] To obtain the defective formation energy, a supercell of α-MoO_3 with 400 atoms was constructed. During the calculations, cut-off energy was set as 500 eV, and optimized atomic geometries were obtained when the forces on each ion was smaller than 0.02 eV $Å^{-1}$.

Acknowledgements

The authors acknowledge the financial support from the National Key Research and Development Program (2021YFA0717600), the National Natural Science Foundation of China (Nos. 62121005, 62022081, and 61974099), the Natural Science Foundation of Jilin Province (20210101173JC), and Changchun Key Research and Development Program (21ZY03). H.Z. acknowledges the support from the Youth Innovation Promotion Association CAS and the Key Research Program of Frontier Sciences, Chinese Academy of Sciences (No. ZDBS-LY-JSC015).

Conflict of Interest

The authors declare no conflict of interest.

Open Research

Data Availability Statement

The data that support the findings of this study are available from the corresponding author upon reasonable request.

Supporting Information

Filename	Description
adom202300180-sup-0001-SuppMat.pdf 1.2 MB	Supporting Information

Please note: The publisher is not responsible for the content or functionality of any supporting information supplied by the authors. Any queries (other than missing content) should be directed

to the corresponding author for the article.

References

1 W. Ma, P. Alonso-Gonzalez, S. Li, A. Y. Nikitin, J. Yuan, J. Martin-Sanchez, J. Taboada-Gutierrez, I. Amenabar, P. Li, S. Velez, C. Tollan, Z. Dai, Y. Zhang, S. Sriram, K. Kalantar-Zadeh, S. T. Lee, R. Hillenbrand, Q. Bao, *Nature* 2018, **562**, 557.

CAS | PubMed | Web of Science® | Google Scholar

2 J. D. Caldwell, O. J. Glembocki, Y. Francescato, N. Sharac, V. Giannini, F. J. Bezares, J. P. Long, J. C. Owrutsky, I. Vurgaftman, J. G. Tischler, V. D. Wheeler, N. D. Bassim, L. M. Shirey, R. Kasica, S. A. Maier, *Nano Lett.* 2013, **13**, 3690.

CAS | PubMed | Web of Science® | Google Scholar

3 A. J. Giles, S. Dai, I. Vurgaftman, T. Hoffman, S. Liu, L. Lindsay, C. T. Ellis, N. Assefa, I. Chatzakis, T. L. Reinecke, J. G. Tischler, M. M. Fogler, J. H. Edgar, D. N. Basov, J. D. Caldwell, *Nat. Mater.* 2018, **17**, 134.

CAS | PubMed | Web of Science® | Google Scholar

4 S. Dai, Z. Fei, Q. Ma, A. S. Rodin, M. Wagner, A. S. McLeod, M. K. Liu, W. Gannett, W. Regan, K. Watanabe, T. Taniguchi, M. Thiemens, G. Dominguez, A. H. Castro Neto, A. Zettl, F. Keilmann, P. Jarillo-Herrero, M. M. Fogler, D. N. Basov, *Science* 2014, **343**, 1125.

CAS | PubMed | Web of Science® | Google Scholar

5 P. Li, M. Lewin, A. V. Kretinin, J. D. Caldwell, K. S. Novoselov, T. Taniguchi, K. Watanabe, F. Gaussmann, T. Taubner, *Nat. Commun.* 2015, **6**, 7507.

CAS | PubMed | Web of Science® | Google Scholar

6 M. Autore, P. Li, I. Dolado, F. J. Alfaro-Mozaz, R. Esteban, A. Atxabal, F. Casanova, L. E. Hueso, P. Alonso-Gonzalez, J. Aizpurua, A. Y. Nikitin, S. Velez, R. Hillenbrand, *Light: Sci. Appl.* 2018, **7**, 17172.

CAS | PubMed | Web of Science® | Google Scholar

7 W. Lyu, H. Teng, C. Wu, X. Zhang, X. Guo, X. Yang, Q. Dai, *Nanoscale* 2021, **13**, 12720.

PubMed | Web of Science® | Google Scholar

8 S. Dai, Q. Ma, T. Andersen, A. S. McLeod, Z. Fei, M. K. Liu, M. Wagner, K. Watanabe, T. Taniguchi, M. Thiemens, F. Keilmann, P. Jarillo-Herrero, M. M. Fogler, D. N. Basov, *Nat. Commun.* 2015, **6**, 6963.

CAS | PubMed | Web of Science® | Google Scholar

9 Z. W. Liu, H. Lee, Y. Xiong, C. Sun, X. Zhang, *Science* 2007, **315**, 1686.

CAS | PubMed | Web of Science® | Google Scholar

10 B. Neuner III, D. Korobkin, C. Fietz, D. Carole, G. Ferro, G. Shvets, *J. Phys. Chem. C* 2010, **114**, 7489.

CAS | Web of Science® | Google Scholar

11 N. Bareza, B. Paulillo, T. M. Slipchenko, M. Autore, I. Dolado, S. Liu, J. H. Edgar, S. Velez, L. Martin-Moreno, R. Hillenbrand, V. Pruneri, *ACS Photonics* 2022, **9**, 34.

CAS | Web of Science® | Google Scholar

12 J. D. Caldwell, L. Lindsay, V. Giannini, I. Vurgaftman, T. L. Reinecke, S. A. Maier, O. J. Glembocki, *Nat. Photonics* 2015, **4**, 44.

CAS | Google Scholar

13 T. Low, A. Chaves, J. D. Caldwell, A. Kumar, N. X. Fang, P. Avouris, T. F. Heinz, F. Guinea, L. Martin-Moreno, F. Koppens, *Nat. Mater.* 2017, **16**, 182.

CAS | PubMed | Web of Science® | Google Scholar

14 R. Hillenbrand, T. Taubner, F. Keilmann, *Nature* 2002, **418**, 159.

CAS | PubMed | Web of Science® | Google Scholar

15 S. Kitade, A. Yamada, I. Morichika, K. Yabana, S. Ashihara, *ACS Photonics* 2021, **8**, 152.

CAS | Web of Science® | Google Scholar

16 D. Z. A. Chen, G. Chen, *Appl. Phys. Lett.* 2007, **91**, 121906.

Web of Science® | Google Scholar

17 S. Tachikawa, J. Ordonez-Miranda, Y. Wu, L. Jalabert, R. Anufriev, S. Volz, M. Nomura, *Appl. Phys. Lett.* 2022, **121**, 202202.

CAS | Google Scholar

18 G. Hu, W. Ma, D. Hu, J. Wu, C. Zheng, K. Liu, X. Zhang, X. Ni, J. Chen, X. Zhang, Q. Dai, J. D. Caldwell, A. Paarmann, A. Alo, P. Li, C.-W. Qiu, *Nat. Nanotechnol.* 2022, **18**, 64.

PubMed | Web of Science® | Google Scholar

19 N. C. Passler, X. Ni, G. W. Hu, J. R. Matson, G. Carini, M. Wolf, M. Schubert, A. Alu, J. D. Caldwell, T. G. Folland, A. Paarmann, *Nature* 2022, **602**, 595.

CAS | PubMed | Web of Science® | Google Scholar

20 R. Geick, C. H. Perry, G. Rupprecht, *Phys. Rev.* 1966, **146**, 543.

CAS | Web of Science® | Google Scholar

21 J. D. Caldwell, A. V. Kretinin, Y. G. Chen, V. Giannini, M. M. Fogler, Y. Francescato, C. T. Ellis, J. G. Tischler, C. R. Woods, A. J. Giles, M. Hong, K. Watanabe, T. Taniguchi, S. A. Maier, K. S. Novoselov, *Nat. Commun.* 2014, **5**, 5221.

CAS | PubMed | Web of Science® | Google Scholar

22 D. N. Basov, M. M. Fogler, F. J. G. d. Abajo, *Science* 2016, **354**, 1992.

Web of Science® | Google Scholar

23 E. E. Narimanov, A. V. Kildishev, *Nat. Photonics* 2015, **9**, 214.

CAS | Web of Science® | Google Scholar

24 Z. Zheng, J. Jiang, N. Xu, X. Wang, W. Huang, Y. Ke, S. Zhang, H. Chen, S. Deng, *Adv. Mater.* 2022, **34**, 2104164.

CAS | Web of Science® | Google Scholar

25 Q. Zhang, Q. Ou, G. Hu, J. Liu, Z. Dai, M. S. Fuhrer, Q. Bao, C. W. Qiu, *Nano Lett.* 2021, **21**, 3112.

CAS | PubMed | Web of Science® | Google Scholar

26 A. Bapat, S. Dixit, Y. Gupta, T. Low, A. Kumar, *Nat. Photonics* 2022, **11**, 2329.

CAS | Google Scholar

27 M. A. Py, P. E. Schmid, J. T. Vallin, *Nuovo Cimento Della Societa Italiana Di Fisica B-General Physics Relativity Astronomy and Mathematical Physics and Methods* 1977, **38**, 271.

Google Scholar

28 S. Abedini Dereshgi, T. G. Folland, A. A. Murthy, X. Song, I. Tanriover, V. P. Dravid, J. D. Caldwell, K. Aydin, *Nat. Commun.* 2020, **11**, 5771.

CAS | PubMed | Web of Science® | Google Scholar

29 W. Ma, G. Hu, D. Hu, R. Chen, T. Sun, X. Zhang, Q. Dai, Y. Zeng, A. Alu, C. W. Qiu, P. Li, *Nature* 2021, **596**, 362.

CAS | PubMed | Web of Science® | Google Scholar

30 M. Chen, X. Lin, T. H. Dinh, Z. Zheng, J. Shen, Q. Ma, H. Chen, P. Jarillo-Herrero, S. Dai, *Nat. Mater.* 2020, **19**, 1307.

CAS | PubMed | Web of Science® | Google Scholar

31 J. Duan, N. Capote-Robayna, J. Taboada-Gutierrez, G. Alvarez-Perez, I. Prieto, J. Martin-Sanchez, A. Y. Nikitin, P. Alonso-Gonzalez, *Nano Lett.* 2020, **20**, 5323.

CAS | PubMed | Web of Science® | Google Scholar

32 G. Hu, Q. Ou, G. Si, Y. Wu, J. Wu, Z. Dai, A. Krasnok, Y. Mazor, Q. Zhang, Q. Bao, C. W. Qiu, A. Alu, *Nature* 2020, **582**, 209.

CAS | PubMed | Web of Science® | Google Scholar

33 Z. Zheng, F. Sun, W. Huang, J. Jiang, R. Zhan, Y. Ke, H. Chen, S. Deng, *Nano Lett.* 2020, **20**, 5301.

CAS | PubMed | Web of Science® | Google Scholar

34 Z. Dai, G. Hu, G. Si, Q. Ou, Q. Zhang, S. Balendhran, F. Rahman, B. Y. Zhang, J. Z. Ou, G. Li, A. Alu, C. W. Qiu, Q. Bao, *Nat. Commun.* 2020, **11**, 6086.

CAS | PubMed | Web of Science® | Google Scholar

35 W. Huang, F. Sun, Z. Zheng, T. G. Folland, X. Chen, H. Liao, N. Xu, J. D. Caldwell, H. Chen, S. Deng, *Adv. Sci.* 2021, **8**, 2004872.

CAS | Google Scholar

36 Z. Fei, A. S. Rodin, G. O. Andreev, W. Bao, A. S. McLeod, M. Wagner, L. M. Zhang, Z. Zhao, M. Thiemens, G. Dominguez, M. M. Fogler, A. H. Castro Neto, C. N. Lau, F. Keilmann, D. N. Basov, *Nature* 2012, **487**, 82.

CAS | PubMed | Web of Science® | Google Scholar

37 W. Luo, A. B. Kuzmenko, J. Qi, N. Zhang, W. Wu, M. Ren, X. Zhang, W. Cai, J. Xu, *Nano Lett.* 2021, **21**, 5151.

CAS | PubMed | Web of Science® | Google Scholar

38 B. C. Yao, Y. Liu, S. W. Huang, C. Choi, Z. D. Xie, J. F. Flores, Y. Wu, M. B. Yu, D. L. Kwong, Y. Huang, Y. J. Rao, X. F. Duan, C. W. Wong, *Nat. Photonics* 2018, **12**, 22.

CAS | Web of Science® | Google Scholar

39 J. Chen, M. Badioli, P. Alonso-Gonzalez, S. Thongrattanasiri, F. Huth, J. Osmond, M. Spasenovic, A. Centeno, A. Pesquera, P. Godignon, A. Zurutuza Elorza, N. Camara, F. Javier Garcia de Abajo, R. Hillenbrand, F. H. L. Koppens, *Nature* 2012, **487**, 77.

CAS | PubMed | Web of Science® | Google Scholar

40 Y. Wu, Q. Ou, Y. Yin, Y. Li, W. Ma, W. Yu, G. Liu, X. Cui, X. Bao, J. Duan, G. Álvarez-Pérez, Z. Dai, B. Shabbir, N. Medhekar, X. Li, C.-M. Li, P. Alonso-González, Q. Bao, *Nat. Commun.* 2020, **11**, 2646.

CAS | PubMed | Web of Science® | Google Scholar

41 Y. L. Zeng, Q. D. Ou, L. Liu, C. Q. Zheng, Z. Y. Wang, Y. N. Gong, X. Liang, Y. P. Zhang, G. W. Hu, Z. L. Yang, C. W. Qiu, Q. L. Bao, H. Y. Chen, Z. G. Dai, *Nano Lett.* 2022, **22**, 4260.

CAS | PubMed | Web of Science® | Google Scholar

42 H. Hu, N. Chen, H. C. Teng, R. W. Yu, Y. P. Qu, J. Z. Sun, M. F. Xue, D. B. Hu, B. Wu, C. Li, J. N. Chen, M. K. Liu, Z. P. Sun, Y. Q. Liu, P. N. Li, S. H. Fan, F. J. G. de Abajo, Q. Dai, *Nat. Nanotechnol.* 2022, **17**, 940.

CAS | PubMed | Web of Science® | Google Scholar

43 Z. Zheng, J. Chen, Y. Wang, X. Wang, X. Chen, P. Liu, J. Xu, W. Xie, H. Chen, S. Deng, N. Xu, *Adv. Mater.* 2018, **30**, 1705318.

Web of Science® | Google Scholar

44 A. M. Dubrovkin, B. Qiang, T. Salim, D. Nam, N. I. Zheludev, Q. J. Wang, *Nat. Commun.* 2020, **11**, 1863.

CAS | PubMed | Web of Science® | Google Scholar

45 T. C. Sum, A. A. Bettiol, J. A. van Kan, F. Watt, E. Y. B. Pun, K. K. Tung, *Appl. Phys. Lett.* 2003, **83**, 1707.

CAS | Web of Science® | Google Scholar

46 A. Roberts, M. L. vonBibra, *J. Lightwave Technol.* 1996, **14**, 2554.

CAS | Web of Science® | Google Scholar

47 K. Liu, E. Y. B. Pun, T. C. Sum, A. A. Bettiol, J. A. van Kan, F. Watt, *Appl. Phys. Lett.* 2004, **84**, 684.